

## COHERENT TRANSPORT OF LIGHT IN COLD ATOMS

GUILLAUME LABEYRIE

*Institut Non Linéaire de Nice, UMR 6618 CNRS,  
1361 route des Lucioles, 06560 Valbonne, France  
guillaume.labeyrie@inln.cnrs.fr*

Received 31 October 2007

We present an overview of the investigations on the transport of near-resonant light in laser-cooled atomic vapors, a field that emerged during the past decade. We first discuss time-resolved measurements yielding some informations on the nature of this transport, which is quasi-diffusive for low temperatures and limited optical thicknesses. We then focus on the coherence of the transport, which is probed using the coherent backscattering interference. We identify and analyze in detail several mechanisms limiting the coherence length in such media.

*Keywords:* Cold atoms; coherent transport of light; coherent backscattering.

### 1. Introduction

Coherent wave transport in disordered scattering media has been the object of an intense scrutiny for the past decades. This interest was initially fuelled by the possibility to observe interferential corrections to the usual diffusive transport. For very strongly scattering media, interferences are expected to induce in 3D a phase transition between a conducting state (usual diffusive transport) and an insulating state (strong or Anderson localization<sup>1</sup>) where transport is suppressed and waves exist inside the medium in localized states.

The universal character of this physical situation makes it relevant for a vast variety of wave-scatterer systems: seismic waves in the earth crust,<sup>2</sup> acoustic waves,<sup>3</sup> electronic waves in metals or semi-conductors,<sup>4</sup> atomic matter waves in disordered light potentials,<sup>5</sup> microwaves<sup>6</sup> and light waves scattering off various media ranging from milk to interplanetary dust.<sup>7</sup> Electromagnetic waves have emerged as an appropriate tool to study localization effects due to the non-interacting character of photons and the flexibility they offer in experiments. Strong localization was observed with microwaves in quasi-1D systems,<sup>6</sup> and also reported for light in 3D.<sup>8</sup> Recent experimental results now provide quite convincing evidence for strong localization of light in 3D.<sup>9</sup>

Among the great variety of scattering media employed to study light transport, cold atomic vapors have recently appeared.<sup>10</sup> Several unusual properties initially motivated our interest in such “exotic” scattering media. First, atoms behave like

true point scatterers. It is possible to start from the accurate microscopic description of an atom to derive the full mesoscopic transport properties of large samples. Cold atomic ensembles constitute very “pure” samples, without the polydispersivity and defects that usually plague solid-state physics samples. For instance, the absence of absorption is a definite advantage when looking for signatures of strong localization.<sup>8</sup> Cold atoms are known for the degree of control and the possibility of parameter tuning that can be achieved in experiments. As an example, the very sharp resonance of the atomic scatterer allows for a continuous, external tuning of the scattering cross-section via the light frequency over orders of magnitude. It is thus in principle possible e.g. to continuously tune the system across the Anderson transition without actually modifying the sample. However, as will be seen, this strong resonance also has the drawback to enhance the sample sensitivity to decoherence processes.

The present paper reviews the results obtained during the last years on transport of light in cold atomic vapors. Section 2 provides a short description of the typical experimental scheme. Section 3 summarizes results on diffusive transport and radiation trapping (RT) of light in cold atomic samples. We then specifically address in Sec. 4 the issue of the *coherence* of the transport, which is probed using the coherent backscattering (CBS) interference. We identify and analyze three decoherence mechanisms present in such media: Sec. 4.2 describes the role of the atomic internal structure, Sec. 4.3 is devoted to the impact of the residual atomic motion, and Sec. 4.4 treats the situation of CBS in the non-linear regime.

## 2. Experimental Setup

Figure 1 illustrates the typical experimental scheme, with the example of a coherent backscattering measurement (see Sec. 4.1). The cold atomic cloud is prepared in a magneto-optical trap (MOT). The atoms are trapped and cooled by the application of six laser beams detuned to the red of the  $F = 3 \rightarrow F' = 4$  dipole transition of the D2 line of Rb<sup>85</sup> (wavelength  $\lambda = 780$  nm, natural width  $\Gamma/2\pi = 5.9$  MHz). The same transition will be employed for all the transport experiments presented here. Up to  $2 \times 10^{10}$  atoms are trapped in a quasi-Gaussian cloud of FWHM size  $E \approx 6$  mm at a temperature of 40  $\mu$ K. The corresponding 1D *rms* velocity is  $v = 6.5$  cm/s.

Prior to all measurements, the atoms are released from the trap by switching off the trapping lasers and magnetic field. Approximately 1 ms later, a probe laser beam is turned on shortly (typical duration  $< 200$   $\mu$ s) to illuminate the atoms and perform the measurement. To study multiple scattering of light, it is necessary to obtain a sample of large *optical thickness*  $b = E/\ell > 1$ , where  $\ell$  is the mean-free path. Due to the resonant scattering cross-section, the optical thickness is

$$b(\delta) = \frac{b(0)}{1 + 4(\delta/\Gamma)^2}, \quad (1)$$

where  $\delta = \omega - \omega_0$  is the light detuning from resonance ( $\omega$  and  $\omega_0$  are the light

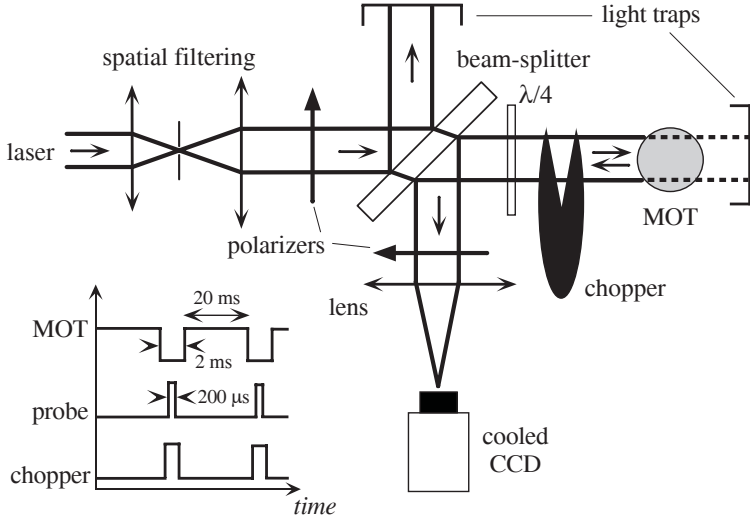


Fig. 1. Experimental set-up for coherent backscattering. The cold atomic cloud is released from the MOT, and then illuminated by a collimated laser beam. The backscattered intensity is collected by a beam-splitter and its angular distribution recorded on a cooled CCD. The MOT is then turned back on to recapture the atoms. The image is accumulated over several thousand such cycles, thanks to a synchronized chopper which blocks the detection during the MOT phase.

and atomic resonance angular frequencies respectively). For resonant light ( $\delta = 0$ ), the maximum optical thickness of our Rubidium cloud is  $b \simeq 40$ , with a minimum mean-free path  $\ell \approx 130 \mu\text{m}$  at the center of the cloud. We are thus working in the *weak scattering regime* with  $k\ell \gg 1$  ( $k = 2\pi/\lambda$  is the light wavenumber).

In the case of a CBS measurement, the backscattered light is collected by a beam-splitter and the far-field distribution imaged on a Peltier-cooled CCD placed in the focal plane of a lens. The angular resolution of the apparatus is 0.1 mrad, one order of magnitude below the typical CBS width.

After 2 ms, the MOT is switched back on to prevent the atoms from escaping the trapping area. It is necessary to accumulate the CBS signal over several thousands cycles in order to obtain a good signal to noise ratio. To this end, we use a synchronized chopper wheel which blocks all light to the CCD during the MOT's operation and opens only during the CBS acquisition period. The CCD thus remains in acquisition mode all the time but accumulates photons only during the illumination of the cloud by the probe laser.

### 3. Transport Regimes in Cold Atoms

This section is devoted to the study of the diffusive-like transport regimes for near-resonant light in cold atomic vapors. In standard opaque media such as e.g. white paint where scattering is *elastic*, the transport is diffusive for optically-thick samples  $b \gg 1$ . At the other end of the spectrum lies the transport of resonant radiation

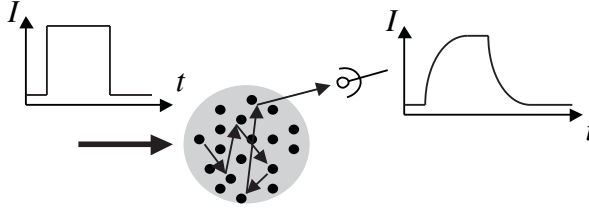


Fig. 2. Principle of radiation trapping experiment. A pulsed laser beam illuminates the sample. A detector monitors the decay of the diffuse light once the excitation has been switched off.

in hot vapors, which has been the subject of an extensive research for nearly a century. There, the *frequency redistribution* due to the motion of the scatterers (inhomogeneous Doppler broadening) or to collisions (homogeneous broadening) deeply affects the transport, which is no longer diffusive as first pointed out by Kenty in 1932.<sup>11</sup> In the “Doppler regime” where inhomogeneous broadening dominates, it was shown by Holstein<sup>12</sup> that one can quite accurately describe the transport by assuming that the light frequency before and after a scattering event are completely decorrelated (complete frequency redistribution). More involved theories (partial frequency redistribution) were later developed to deal with a larger range of gas temperature and pressure (see e.g. Ref. 13). With the advent of laser cooling in the 80s, it became possible to produce vapors with negligible collisions where the inhomogeneous width is well below the natural (homogenous) width. We present in this section the first extensive study of transport in this new regime.

To study dynamical features of the transport such as e.g. the diffusion coefficient, we employed the “radiation trapping” scheme sketched in Fig. 2. This technique has been employed to diagnose strong localization in Ref. 9, and was first applied to cold atomic vapors in Ref. 14. The sample is illuminated by a pulsed (rectangular) probe beam, and we monitor the decay of the diffuse light after the excitation has been switched off. In the elastic case, the residence time of photons inside the sample is proportional to the number of scattering events, which increases quadratically with the optical thickness  $b$ . More quantitatively, the long-time decay of diffuse intensity is exponential with a time constant:

$$\tau_0^{el} = \frac{3}{\alpha\pi^2} b^2 \tau_{tr} \quad (2)$$

where  $\alpha$  is a geometry-dependent numerical factor ( $\alpha = 1$  for a slab, 4 for a homogenous sphere and 5.35 for an inhomogeneous sphere with a Gaussian density profile<sup>15</sup>) and  $\tau_{tr}$  is the *transport time*, the average time delay between two successive scattering events. Equation (2) is valid in the diffusive regime  $b \gg 1$ . Figure 3 shows the result of such an experiment realized with an cold ( $T = 40 \mu\text{K}$ ) cloud of Rb<sup>85</sup>.<sup>15</sup> The incident light is resonant with the atomic transition ( $\delta = 0$ ), and the optical thickness is varied by adjusting the number of trapped atoms.

Figure 3(A) reports examples of diffuse intensity decays for various values of the optical thickness (note the semi-log scale). The initial, steady-state value of

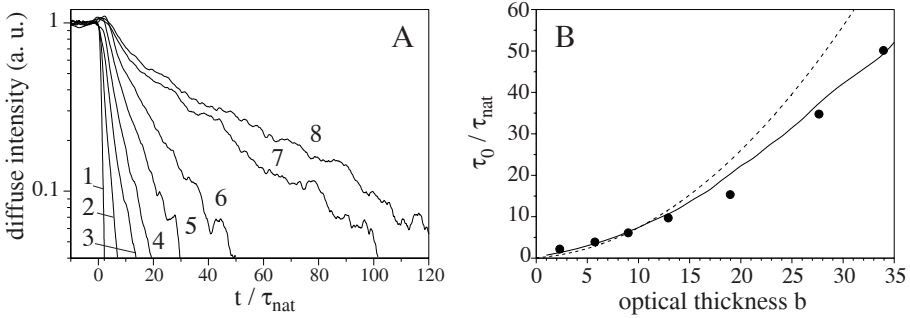


Fig. 3. Radiation trapping in cold atoms. (A): Diffuse intensity decay for various optical thicknesses. 1: probe pulse; 2:  $b = 2$ ; 3:  $b = 6$ ; 4:  $b = 9$ ; 5:  $b = 13$ ; 6:  $b = 19$ ; 7:  $b = 28$ ; 8:  $b = 34$ . (B): Late-time decay constants  $\tau_0$ . Experiment (circles), elastic diffusion theory (dashed line) and MC simulation including the residual atomic motion (solid line).

the detected signal has been scaled to unity for all values of  $b$ . The detection time is expressed in units of the excited state lifetime  $\tau_{nat} = \Gamma^{-1} = 27$  ns (the zero corresponds to the shut-off of the excitation). Trace 1 corresponds to the probe laser temporal profile in the absence of atoms. The observed decays (traces 2 to 8) are all found to be exponential after an initial transient. By fitting the late decay to an exponential, we extract the time-constant  $\tau_0$  which is plotted in Fig. 3(B) (circles). It increases nearly quadratically as expected from diffusion theory (Eq. (2), dashed line) up to roughly  $b = 12$ . However, above this value a clear departure from the elastic diffusion theory is observed with a faster decrease of the diffuse intensity. This is attributed to the small frequency redistribution due to the residual motion of the atoms, as confirmed by the Monte Carlo (MC) simulation (solid line). The interpretation is rather simple: although a single scattering event results in a very small random frequency redistribution  $kv/\Gamma \approx 2 \times 10^{-2}$ , the *cumulative* impact of  $N$  successive scatterings can become non-negligible. Assuming uncorrelated successive frequency redistribution events, the average frequency redistribution after  $N \gg 1$  scatterings is  $\langle \Delta\omega \rangle = \sqrt{D_\omega N \Gamma^{-1}}$ , where  $D_\omega = 2(kv)^2 \Gamma$  is the *frequency diffusion coefficient*.<sup>16</sup> Roughly speaking, this frequency diffusion is expected to significantly affect the transport when  $\langle \Delta\omega \rangle \approx \Gamma/2$ . This occurs after  $N = 1/8(kv/\Gamma)^{-2} \approx 300$  scatterings, which corresponds to  $b \approx 17$  since the average number of scattering events is  $N \simeq b^2$ . The order of magnitude given by this rough estimation is correct, and we see on Fig. 3(B) that the quantitative agreement with the MC simulation is very good.

Thus, because of the residual atomic motion resulting in a slightly *inelastic* scattering, the transport can not be considered strictly diffusive as pointed out by Holstein.<sup>12</sup> However, the diffusive nature of the transport is not deeply affected as long as  $bkv < \Gamma$ . This is a new regime of “frequency diffusion” where modifications of the transport are driven by a large number of small random frequency kicks. On the contrary for  $bkv \gg \Gamma$  (Doppler regime) large deviations from diffusive transport are expected.

Let us first consider the “quasi-elastic” case  $bkv \ll \Gamma$ . Since the transport is not substantially affected by Doppler-induced frequency redistribution, we employ the formalism of the diffusion theory. From the data of Fig. 3 and the measured values of the mean-free path  $\ell$ , we can extract the transport time:  $\tau_{tr} \simeq \tau_{nat}$ . The transport time is thus equal to the atomic excited state lifetime. This time is very long (27 ns) compared to usual, non-resonant samples where  $\tau_{tr} \approx \ell/c < 1\text{ps}$  for  $\ell = 100 \mu\text{m}$ ! This is a direct consequence of the very sharp resonance of the atomic scatterer. We have shown experimentally<sup>15</sup> that  $\tau_{tr}$  is roughly *frequency-independent* in the vicinity of the resonance, a property predicted by the theory of point scatterers.<sup>17</sup> This non-trivial behavior originates in the compensation of the two contributions to the transport time:

$$\tau_{tr}(\delta) = \tau_W(\delta) + \frac{\ell(\delta)}{v_g(\delta)}. \quad (3)$$

The first term is the scattering Wigner time, which represents the time delay upon scattering of a quasi-monochromatic wavepacket of spectral width  $\ll \Gamma$ . It is maximum on resonance  $\tau_W(\delta = 0) = 2/\Gamma$  and decreases as a Lorentzian when  $|\delta|$  increases. The second term represents the propagation up to the next scatterer, in the *effective* medium characterized by a refractive index  $n$ . This propagation is accomplished at the group velocity  $v_g$ . Due to the anomalous dispersion of a two-level system, the group velocity is negative (with modulus  $\ll c$ ) on resonance,<sup>18</sup> and positive  $\approx c$  away from resonance ( $\delta \gg \Gamma$ ). Note that the variations of the two terms compensate only in a limited frequency range around resonance: in the limit of large detunings,  $\tau_W \rightarrow 0$  while  $\ell/v_g$  increases quadratically.

Another interesting quantity is the *energy transport velocity*  $v_{tr} = \ell/\tau_{tr}$ , which describes the velocity of the energy in the diffuse light. In contrast to the group velocity,  $v_{tr}$  is always positive and  $\approx c$  in most samples. Using our measured values of  $\tau_{tr}$  and  $\ell$ , we obtain  $v_{tr} \approx 3 \times 10^{-5}c$ . This extremely low value is a direct consequence of the sharp atomic resonance which also yields the very long transport time. The reduction of the transport velocity when using resonant scatterers was first demonstrated in Ref. 19. This *slowed energy transport* is also reflected by the small value of the spatial diffusion coefficient  $D = \ell^2/(3\tau_{tr}) = 0.66 \text{ m}^2/\text{s}$ . Similar values were reported in Ref. 20, where the authors studied the time-dependence of the light depolarization. This slow transport should not be mistaken with the “slow light” of Ref. 21, where the *group velocity* is reduced by manipulating the atomic dispersion.

Let us now turn back to the frequency diffusion phenomenon. Its clearest illustration is obtained for a detuned excitation, as represented in Fig. 4. We report in Fig. 4(A) the diffuse intensity decay for  $\delta = +1.5\Gamma$  and different *rms* atomic velocities (1:  $v = 0.087 \text{ m/s}$ ; 2:  $v = 0.24 \text{ m/s}$ ; 3:  $v = 0.99 \text{ m/s}$ ). The noisy curves are the experimental data and the lines the MC simulations. In contrast to the resonant case (Fig. 3), the decay is now clearly non-exponential. Furthermore, the residence time of photons inside the cloud now seems to increase with  $v$ . The explanation

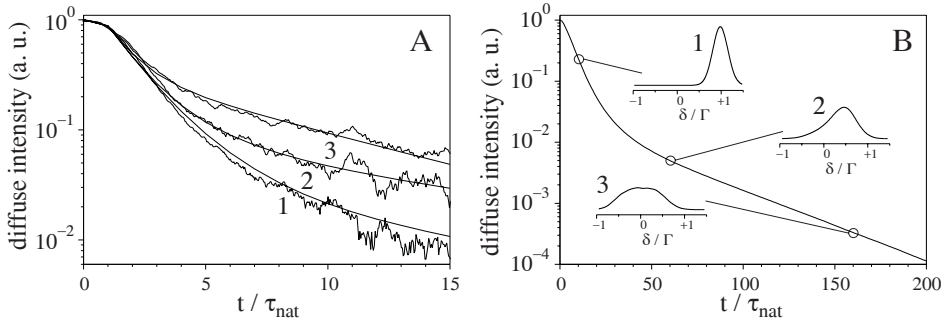


Fig. 4. Observation of frequency diffusion. (A): Diffuse intensity decay for a detuned excitation  $\delta = 1.5\Gamma$  and different *rms* atomic velocities: 1:  $v = 0.087$  m/s; 2:  $v = 0.24$  m/s; 3:  $v = 0.99$  m/s. For each  $v$ , the optical thickness has been adjusted to  $b = 2.2$ . The noisy curves are the experimental data and the lines the MC simulations. (B): Monte Carlo simulation ( $\delta = \Gamma$ ,  $b(\delta) = 6.6$ ,  $v = 0.17$  m/s), with insets showing the evolution of the emerging light spectrum as a function of time.

of this behavior is illustrated in Fig. 4(B), where a MC simulation (monochromatic excitation at  $\delta = \Gamma$ ,  $b(\delta) = 6.6$ ,  $v = 0.17$  m/s) allows us to follow the time-resolved *spectrum* of emerging photons. After a small number of scattering events ( $t/\tau_{\text{nat}} = 10$ ), the emerging light spectrum (inset 1) is nearly Gaussian and centered at the laser frequency ( $\delta = \Gamma$ ). When the number of scatterings increases (inset 2), the spectrum broadens and deforms with a shift towards resonance. At late times, the spectrum is stationary and centered on resonance (inset 3). Indeed, in the course of frequency diffusion part of the photons are shifted away from the resonance and leave the cloud because their mean free path increases. Those shifted closer to resonance see an increased optical thickness and thus experience more scatterings and an increased frequency diffusion rate. This efficient selection process guarantees that ultimately all photons inside the cloud are nearly resonant, whatever the initial laser frequency. The study of RT with a detuned excitation is thus a sensitive technique to study frequency redistribution processes.

Once the photons inside the medium are on resonance (either because of a resonant excitation or as a result of frequency diffusion), the diffuse intensity decay is exponential and governed by the *rms* atomic velocity and the optical thickness. This is illustrated in Fig. 5(A), where we report the measured decay constants ( $\delta = 0$ ) for various *rms* atomic velocities and optical thicknesses:  $b = 30$  (solid circles),  $b = 25$  (open circles),  $b = 13$  (solid squares,  $\times 2$ ) and  $b = 5$  (stars,  $\times 3$ ). The lines correspond to the MC simulations. At fixed  $b$ , the decay is faster when  $v$  increases due to an increased frequency diffusion rate. Figure 5(B) shows the result of MC simulations for a resonant excitation and a slab geometry: the deviation from elastic transport  $1 - \tau_0/\tau_0^{\text{el}}$  is plotted as a function of  $bkv/\Gamma$  (where  $v$  is varied), for different values of the optical thickness:  $b = 10$  (circles),  $b = 20$  (squares) and  $b = 40$  (stars). Here  $\tau_0$  is the decay constant taking into account the atomic velocities, while  $\tau_0^{\text{el}}$  is the elastic decay constant (see Eq. (2)) for the same optical thickness. As can

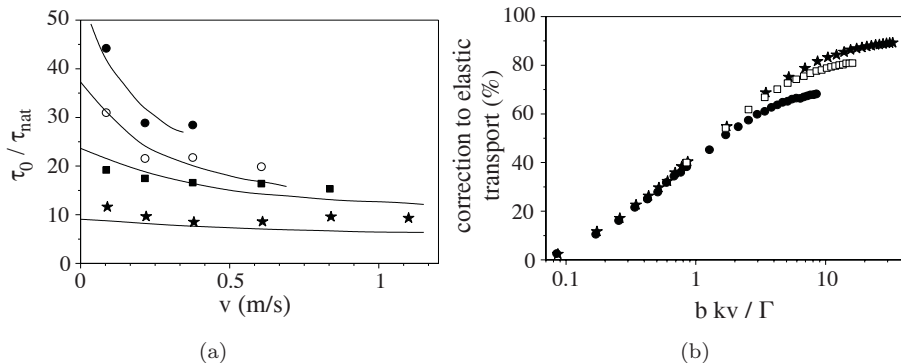


Fig. 5. RT decay versus atomic velocity ( $\delta = 0$ ). (A) Measured RT decay constant versus *rms* atomic velocity for various optical thicknesses:  $b = 30$  (solid circles);  $b = 25$  (open circles);  $b = 13$  (solid squares,  $\times 2$ );  $b = 5$  (stars,  $\times 3$ ). The lines correspond to the MC simulations. (B) Correction to elastic transport  $1 - \tau_0/\tau_0^{\text{el}}$  (see text) as a function of  $bkv/\Gamma$  (where  $v$  is varied) for different values of the optical thickness (MC simulations for a slab geometry):  $b = 10$  (circles),  $b = 20$  (squares) and  $b = 40$  (stars). In the frequency diffusion regime  $bkv/\Gamma < 1$  the decay depends only on the parameter  $bkv/\Gamma$ , while in the Doppler regime  $bkv/\Gamma \gg 1$  it is determined only by  $b$ .

be seen, all curves merge for  $bkv/\Gamma < 1$ : this is the frequency diffusion regime. For  $bkv/\Gamma > 1$  the curves diverge towards asymptotic values determined only by  $b$  (Doppler regime). The frequency diffusion regime thus bridges the gap between two well-documented regimes: the elastic regime ( $v = 0 \rightarrow \tau_0 \propto b^2$ ) and the Doppler regime ( $bkv/\Gamma \gg 1 \rightarrow \tau_0 \propto b\sqrt{\log(b/2)}$ ).<sup>12</sup>

## 4. Coherent Transport

In the previous section, we have seen that the transport of light in cold atomic vapors is quasi-diffusive, at least for moderate optical thicknesses. However, the results presented so far give us no lead on the *coherence* of this transport, although we can expect that the Doppler frequency redistribution will somehow limit this coherence. This issue will be specifically addressed in Sec. 4.3. We thus now turn to the discussion of the coherence of light transport in cold atomic samples.

### 4.1. Coherent backscattering: a probe of coherent transport

The different regimes of wave localization in 3D disordered media are fixed by the value of  $k\ell$ , where  $k$  is the wavenumber and  $\ell$  the transport mean free path. In the most easily accessible weak scattering regime  $k\ell \gg 1$ , interferential corrections to transport are small (weak localization). Strong localization occurs for  $k\ell \lesssim 1$ , a condition known as the Ioffe–Regel criterion.<sup>a</sup> All results reported in the following were obtained in the weak scattering regime, with  $k\ell$  typically  $> 1000$ . Indeed, obtaining dense ( $\simeq 10^{14} \text{ cm}^{-3}$ ) samples of cold atoms is still a fairly involved matter,

<sup>a</sup>In 1D and 2D disordered systems, however, waves are always localized.

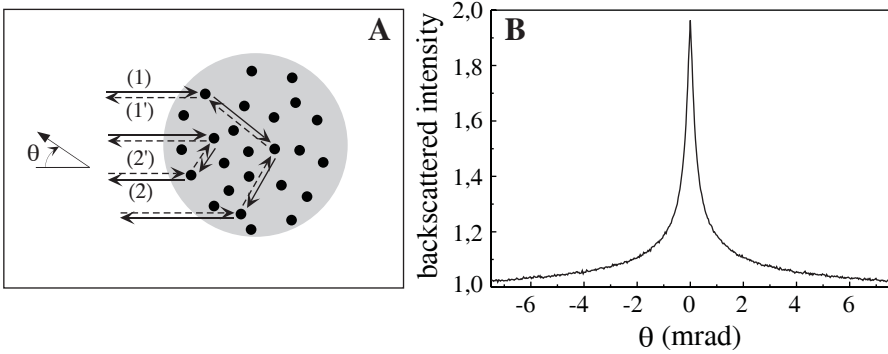


Fig. 6. The CBS effect. (A): The constructive interference between reversed paths e.g. (1) and (1') survives configuration average, while the interference between uncorrelated paths e.g. (1) and (2) vanishes. (B): CBS cone from a sphere of styrofoam (helicity preserving channel).

with densities in standard magneto-optical traps typically 3 orders of magnitude below.

In the weak scattering regime, the main interferential effect is the so-called coherent backscattering. This effect, observed for the first time in the 80s with light,<sup>22</sup> is due to the constructive interference between amplitudes describing *reversed* multiple scattering paths such as (1) and (1') in Fig. 6(A).

These paths follow the same collection of scatterers, but encountered in reverse order. Since the path length difference is zero at exact backscattering ( $\theta = 0$ ), the interference is always constructive. As such, it survives the “configuration” average over the respective positions of the scatterers. This is not the case for *decorrelated* paths such as (1) and (2), whose interference will wash out during configuration average.

CBS manifests itself as a narrow peak in the configuration-averaged scattered light intensity distribution, centered at the direction of exact backscattering. An example obtained from a slowly rotating sphere of styrofoam is shown in Fig. 6(B). The interference contrast drops rapidly away from backscattering because of the position-dependent phase shift (between reversed amplitudes) arising for  $\theta \neq 0$ . The CBS peak is thus characterized by a narrow angular width  $\Delta\theta \approx (k\ell)^{-1}$ . Its height is quantified by the CBS enhancement factor, defined for  $\theta = 0$ :

$$\eta = 1 + \frac{C}{S + L}, \quad (4)$$

where  $C$  is the interference term (decaying rapidly for  $\theta \neq 0$ ) and  $L$  the average diffuse intensity (no interference contribution).  $S$  is the single scattering term, which contributes to the total intensity but not to the CBS interference.  $C/L$  is the interference contrast and a direct measure of the mutual coherence between reversed paths. If this coherence is perfect, one has a maximum contrast  $C/L = 1$ , and if in addition single scattering can be removed ( $S = 0$ ) then  $\eta = 2$ . In “classical” samples

of spherically-symmetric scatterers, both conditions are fulfilled in the so-called “helicity preserving channel” ( $h\parallel h$ ) where both incoming and detected polarizations are circular with the same helicity.

The CBS signal can be viewed as originating from e.g. a collection of self-aligned, zero path-length difference Michelson interferometers, with a certain distribution of arm lengths corresponding to the lengths of multiple scattering paths inside the disordered sample. The interference contrast is thus only sensitive to *decoherence* processes occurring *during* the transport. Typically, this will induce an exponential decay of the interference contrast as the length of a multiple scattering path is increased:

$$\frac{C}{L}(N) = e^{-N/N_\Phi}, \quad (5)$$

where  $N$  is the number of scattering events and  $N_\Phi$  represents the number of scattering events over which the coherence is lost. The corresponding distance of diffusive transport is the *coherence length*  $L_\Phi = \sqrt{DN_\Phi\tau_{tr}}$  where  $D = \ell^2/3\tau_{tr}$  is the (spatial) diffusion coefficient and  $\tau_{tr}$  the transport time defined in Sec. 3. We thus obtain:

$$\frac{L_\Phi}{\ell} = \sqrt{\frac{N_\Phi}{3}}. \quad (6)$$

If the size  $E$  of the sample is smaller than  $L_\Phi$ , the coherence is preserved for a typical multiple scattering path inside the sample. In the following, we will refer to this situation as the “mesoscopic regime”. In a standard (i.e. static) CBS experiment, one does not measure directly  $C/L$  as a function of  $N$ , but instead a weighted sum of the contributions of all scattering orders. For instance, in the case of large optical thicknesses, the distribution of scattering orders in the average diffuse intensity is  $P(N) \propto N^{-3/2}$ . If this distribution is *a priori* unknown, one has to rely on a Monte Carlo simulation to determine the  $P(N)$  and extract the coherence length. Note that this problem can in principle be overcome by combining the techniques of CBS and time-resolved detection described in the previous section. Using time-resolved CBS, one can in principle directly measure  $C/L(N)$ . However, this technique has proven difficult to implement due to low photon counting rates.

## 4.2. Internal structure

### 4.2.1. Internal structure and decoherence

Since our first observation of CBS from cold Rb<sup>85</sup> atoms,<sup>10</sup> it was obvious that the enhancement factor is much smaller than 2 in all channels. This is illustrated in Fig. 7, where we report the measured cones (circles) in various polarization channels. The laser is resonant ( $\delta = 0$ ), and the cloud has an optical thickness  $b = 26$ . Quite strikingly, the CBS enhancement factor is *smallest* in the helicity-preserving channel ( $h\parallel h$ ), which yields the maximum value for classical samples as discussed in the previous section. For our Rb<sup>85</sup> atoms, the CBS peak is barely

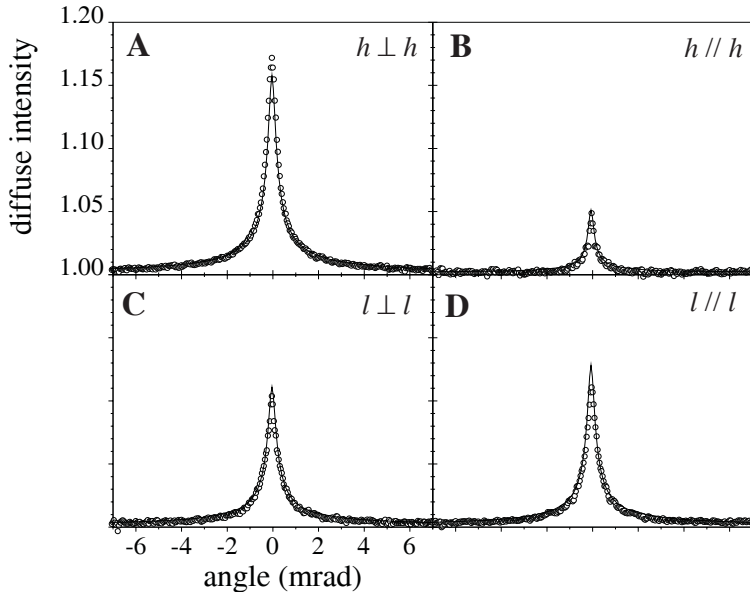


Fig. 7. CBS peaks from an ultra-cold cloud of  $\text{Rb}^{85}$  atoms ( $\delta = 0$ ,  $b = 26$ ), in various polarization channels. Top: circular polarizations orthogonal (A) or parallel (B). Bottom: linear polarizations orthogonal (C) or parallel (D). The symbols correspond to the measured data and the lines to the MC simulations taking into account the geometry of the atomic cloud (no adjustable parameter).

visible in this channel with  $\eta = 1.05$ . This behavior was later confirmed by similar observations in the group of M. Havey.<sup>23</sup>

The explanation for this dramatic interference reduction lies in the internal structure of the atomic ground state.<sup>24</sup> Indeed, the  $F = 3$  state of the D2 line of Rubidium is made of seven degenerate Zeeman sublevels. Thus, the quantum states of the system are described by the polarization of the photon *and* the Zeeman substates of all atoms in the considered multiple scattering path. The CBS signal is a quantum interference between the amplitudes of the two (reversed) paths connecting an initial state (incoming photon polarization + initial atomic internal states) to a final state (outgoing photon polarization + final atomic internal states) which may or not be different from the initial one. The effect of the internal degree of freedom is to introduce an *imbalance* between these amplitudes, thus reducing the interference contrast. This process is illustrated by the example of Fig. 8. We consider two atoms and a  $1/2 \rightarrow 1/2$  transition for the sake of simplicity. In the helicity-preserving channel, the incoming polarization is e.g. right-handed and the detected light is then left-handed. The two atoms are assumed to be in *different* Zeeman substates, and we consider only the case of Rayleigh scattering i.e. no change of internal state occurs due to the scattering of the photon. As can be seen, the amplitude associated with the scattering sequence  $1 \rightarrow 2$  is non-zero while that of the reverse sequence  $2 \rightarrow 1$  is zero. In this extreme case, the interference term

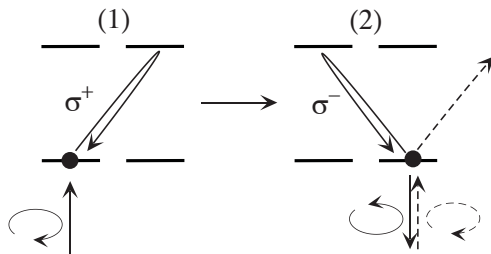


Fig. 8. The impact of internal structure: mechanism for interference reduction. We consider two atoms in different Zeeman substates. The asymmetric response of the atoms with respect to polarization yields different amplitudes for reversed paths, and thus a reduced interference contrast.

vanishes. This loss of interference contrast can also be understood in terms of increased which-path information.<sup>25</sup> Note that in Fig. 8 we have chosen the case of Rayleigh transitions (conserved internal state) to illustrate the impact of the internal structure, but the argument and the conclusions remain valid for “Raman” transitions where the atomic internal state is modified. Whether the CBS signal is dominated by the Rayleigh or Raman contribution depends on the specific transition and polarization channel.<sup>26</sup> The simple example of Fig. 8 illustrates the two necessary conditions for the CBS reduction: first, the atoms should be in *different* Zeeman substates; second, the scattering amplitude for an atom in a given substate should be asymmetric with respect to the light helicity, i.e. different for right and left-handed polarizations. This property, linked to time-reversal symmetry breaking, is always satisfied for a non-zero total angular momentum state. An analog of the effect of the atomic internal structure is found in spin-flip scattering of electrons by magnetic impurities in metals,<sup>27</sup> as will be further discussed in Sec. 4.2.2.

Another, more trivial (but of experimental importance) consequence of the internal structure is the impossibility to reject the single scattering contribution to the backscattered intensity using polarization selection. Because this contribution is typically  $S \approx 40\%$  or higher, this leads to an additional significant reduction of the CBS enhancement according to Eq. (4).

A direct experimental confirmation of the role of the internal structure as a decoherence process was obtained with the observation in our group of the CBS peak from a cold cloud of Sr<sup>88</sup>.<sup>28</sup> This signal, obtained with the  $0 \rightarrow 1$  transition ( $\lambda = 460.7$  nm), is plotted in Fig. 9. Since the atomic ground state has no internal structure, we observe in the  $h\parallel h$  channel an enhancement very close to the theoretical value  $\eta = 2$ . Note that in both Rb and Sr experiments, the residual Doppler effect  $kv/\Gamma$  is similar ( $\approx 2 \times 10^{-2}$ ) and thus can not account for the observed difference of  $\eta$  (see Sec. 4.3).

The impact of the atomic internal structure was formalized in the PhD work of C. Müller, who derived an analytical expression for the CBS interference from dipole transitions between states of arbitrary angular momentum.<sup>26</sup> Generally speaking,

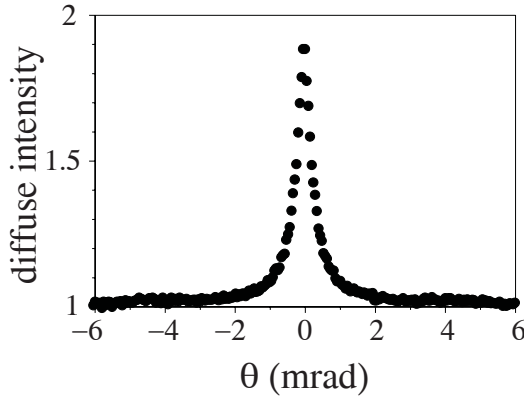


Fig. 9. The impact of internal structure: additional proof. We report the CBS peak measured from a cold cloud of  $\text{Sr}^{88}$  in the  $h\parallel h$  channel, using the  $0 \rightarrow 1$  transition (ground state without internal structure). We observe an enhancement factor very close to the maximal value  $\eta = 2$ .

any transition from a ground state of total angular momentum  $F \neq 0$  yields a small contrast, with the noticeable exception of  $F \rightarrow F$  transitions at large  $F$ . In the case of the  $3 \rightarrow 4$  transition of  $\text{Rb}^{85}$  in the orthogonal helicity channel, the theory predicts  $C/L(N) \propto (19/40)^N$ . This interference reduction due to the internal structure can be interpreted in terms of decoherence. Using Eqs. (5) and (6), we obtain in this case  $L_\phi \approx 0.7\ell$ .

Using the analytical results of Ref. 26, Delande developed an efficient Monte Carlo simulation including all the relevant experimental parameters such as the optical thickness, size and shape of the atomic cloud. Thanks to this effort, a quantitative comparison between theory and experiment could be attempted for the first time, yielding an excellent result<sup>29</sup> as can be seen in Fig. 7 (thin curves). A similar agreement was obtained for the  $2 \rightarrow 3$  transition of  $\text{Rb}^{87}$ .<sup>30</sup> The MC simulation helped to understand the role of the inhomogeneous density distribution in the atomic cloud, which leads to an unusual behavior of the CBS cone width versus mean free path.<sup>31</sup> This is illustrated in Fig. 10(A), where we measured the variation of the CBS cone width  $\Delta\theta$  with light detuning from resonance  $\delta$ . As a consequence of the resonant scattering cross-section, the mean free path varies by a factor of 22 in the course of this experiment. However, it can be seen that  $\Delta\theta$  varies only by a factor 2, while a homogenous medium would yield  $\Delta\theta \propto (k\ell)^{-1}$ . This is because double scattering (which is dominant in the CBS signal) takes place typically at an *optical depth*  $\approx 1$ . For resonant light and large optical thicknesses  $b \gg 1$ , this corresponds to the outer layer of the cloud where the density  $\rho$  is low. When  $\delta$  is increased (i.e. the scattering cross-section decreased), this point moves deeper and deeper inside the cloud where the density increases. Both effects compensate to yield an effective  $\ell = (\sigma\rho)^{-1}$  *nearly frequency-independent*, of the order of the size of the cloud. Figure 10(B) shows the evolution of the CBS enhancement factor. The observed variation is due to the modification of the distribution of

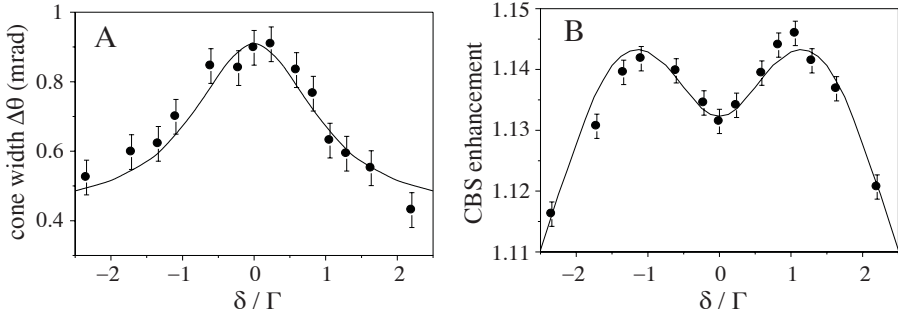


Fig. 10. CBS and light detuning. The CBS signal is recorded as a function of the light detuning from resonance, i.e. for a varying optical thickness of the atomic cloud. (A) Measured CBS peak angular width (symbols) and MC simulation (line). (B) Measured CBS enhancement factor (symbols) and MC simulation (line). Note the slightly asymmetric behavior of the enhancement (see text).

scattering orders, the maximum enhancement corresponding to a maximum double scattering contribution. For a “large” detuning, the optical thickness is small and single scattering dominates which reduces the enhancement (Eq. (4)). For a small  $\delta$ , the respective contribution of higher multiple scattering orders  $N > 2$  is large. Due to the  $(19/40)^N$  decrease of the CBS interference contrast, these scattering orders contribute mainly to  $L$  and not to  $C$ , which reduces the overall enhancement. These mechanisms yield the “double bump” structure of Fig. 10(B). Note the small *asymmetry* of the enhancement with respect to  $\delta$ , with slightly higher values on the “blue” side of the resonance  $\delta > 0$ . This may be an indication of the effect of other accessible excited states in the hyperfine multiplet.<sup>32,33</sup> Although far detuned, the corresponding transitions can yield interference effects which affect the enhancement factor.

#### 4.2.2. *Magneto-optics*

It may thus appear that alkalis, which are the most commonly manipulated atoms, constitute a bad choice to study coherent transport because of their internal structure. As demonstrated in the previous section, the use of the  $0 \rightarrow 1$  transition of  $\text{Sr}^{88}$  solves this problem. However, cooling and trapping Strontium is technically quite demanding, as illustrated by the very few groups using this element in the world.

An alternative approach to the problem of internal structure consists in the application of an external magnetic field, as demonstrated in Ref. 34. This is illustrated in Fig. 11, where we report the CBS enhancement factor measured as a function of the external magnetic field  $B$ . A rapid increase of the interference contrast is observed with  $|B|$ . This observation may seem *a priori* surprising, because the application of a magnetic field breaks time-reversal symmetry and produces a decrease of the CBS interference in classical samples.<sup>35</sup> In our situation, the applied

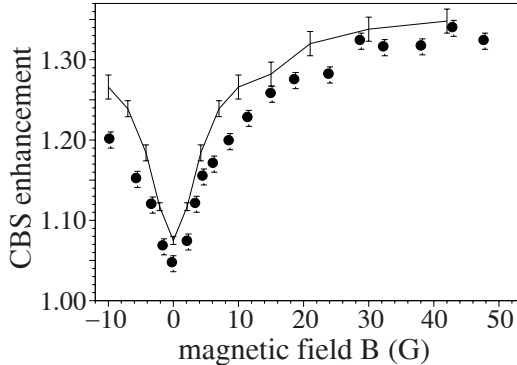


Fig. 11. Coherence restoration by application of a magnetic field. We record the CBS enhancement in the  $h\parallel h$  channel (symbols), as a function of the applied magnetic field. The light frequency is tuned to maintain resonance with the  $m_F = +3 \rightarrow m_F = +4$  transition. The line is the MC simulation.

$B$  field lifts the degeneracy between Zeeman substates, such that optical transitions between given sets of ground and excited substates now occur at different frequencies. If this Zeeman detuning is large enough ( $> \Gamma$ ), one can selectively excite one of these transitions by adjusting the laser frequency. In the experiment of Fig. 11, the laser frequency is tuned to remain in resonance with the  $m_F = +3 \rightarrow m_F = +4$  transition. At our maximum field of 50 G, the closest transition is detuned by  $\approx -2\Gamma$ . This procedure allows us to obtain a quasi-two level system, which yields the maximum interference contrast. Note however that this equivalent two-level system is *oriented*, such that only  $\sigma^+$  can be absorbed or emitted. As a result, the single-scattering contribution cannot be filtered out by polarization selection. This is why the measured enhancement saturates at about 1.35 in Fig. 11. However, the coherence length increases continuously with the applied magnetic field:  $L_\phi \propto \sqrt{B}$ ,<sup>34</sup> as shown by O. Sigwarth in his MC simulation (solid line in Fig. 11). In the situation of Fig. 11, a field of 100 Gauss ( $10^{-2}$  Tesla) is expected to yield  $L_\phi \approx 3\ell$ , i.e. the mutual coherence is lost after roughly 10 scattering events. Even though this effect of coherence restoration is quite spectacular, it is thus of unpractical use to reach large coherence lengths  $L_\phi \gg \ell$ .

This mechanism of coherence restoration is reminiscent of that of conduction electrons in metals, where weak localization corrections to transport are inhibited at zero external  $B$  field due to spin-flip scattering by magnetic impurities.<sup>36</sup> When a  $B$  field is applied, these spin-flip scatterings are suppressed and the coherence is restored.

Because of the sharp atomic resonances and the strong response to an external magnetic field via the Zeeman effect, cold atoms typically boast large magneto-optical properties. This was e.g. illustrated in our group with the observation of Faraday rotation angles of up to  $150^\circ$  with an applied magnetic field of 8 G,<sup>37</sup> which corresponds to a Verdet constant typically 4 orders of magnitude larger than

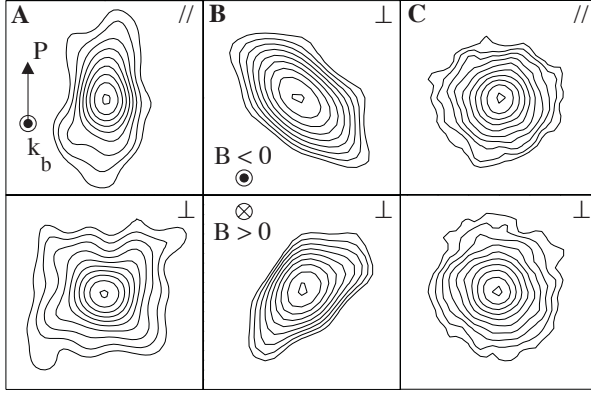


Fig. 12. Hanle effect in CBS. In each quadrant the measured far-field backscattered intensity is plotted as a function of the two azimuthal angles (exact backscattering at center, total range 2 mrad). The incident polarization  $P$  is vertical, the backscattered wavevector  $\mathbf{k}_b$  is pointing towards the reader. (A) Shape of the CBS peak in the  $l||l$  (top) and  $l \perp l$  (bottom) channels, without magnetic field ( $\delta = 0$ ,  $B = 0$ ). (B) When an external magnetic field  $B$  is applied, the CBS peak in the  $l \perp l$  channel flips by  $\pm 45^\circ$  depending on the sign of  $B$  ( $\delta = 0$ ,  $|B| = 8$  G). (C) Same as (A), but with  $B = 10$  G and the light detuned so as to select one pair of ground-excited Zeeman states ( $\delta = 2.6\Gamma$ ).

that of Faraday crystals employed e.g. in optical insulators. A direct manifestation of magneto-optical effect in the CBS interference is illustrated in Fig. 12, with the first observation of the Hanle effect in coherent backscattering.<sup>38</sup> The Hanle effect corresponds to the rotation, under application of a magnetic field, of the dipole induced by a linearly-polarized electromagnetic field inside an atom. As a consequence, the polarization of the light radiated by this atom is rotated with respect to the incident one by an angle  $\Phi(B)$ . This effect can be seen as the microscopic building block for the Faraday effect, which requires the presence of many atoms (effective medium) to become sizeable. CBS is known to be sensitive to the radiation pattern of the scatterers.<sup>39</sup> Indeed, the CBS peak shape is given by the Fourier transform of the diffuse intensity distribution on the front surface of the sample under point-like illumination. At a small number of scattering events ( $N = 2, 3 \dots$ ) this intensity distribution retains some features of the individual radiation pattern, while these features are washed out for  $N \gg 1$  yielding an isotropic distribution. Since CBS is dominated by low-scattering orders, its symmetry can provide direct information on the radiation pattern of individual scatterers.

An example is provided in Fig. 12(A): the dipole radiation pattern produces an elongated CBS peak in the  $l||l$  channel, and a “cushion-shaped” peak in the  $l \perp l$  channel. (These shapes are also observed with small classical scatterers like e.g.  $\text{TiO}_2$  particles.) Let us now consider the case  $N = 2$  with linear incident and detected polarizations forming an angle  $\alpha$ , and resonant light  $\delta = 0$ . One can then derive the angular dependence of the CBS interference: in a polar plot this “CBS radiation pattern” consists of two orthogonal pairs of opposite lobes, with

symmetry axes along the bisectors of the angle formed by the incident and detected polarizations (thus tilted by  $\alpha/2$  and  $(\alpha + \pi)/2$ ). Thus, the symmetry axes of the CBS peak are determined only by  $\alpha$  and independent of  $B$ . However, the *ratio* of the 2 pairs of lobes is  $\propto \tan^4(\alpha/2 - \Phi)$  and thus depends on both  $\alpha$  and  $B$ . In Fig. 12(A),  $\Phi = 0$  ( $B = 0$ ) and  $\alpha/2 = 0$  (top) or  $\pi/4$  (bottom). The earlier case yields vertical and horizontal symmetry axes and only one pair of lobes, which corresponds to an elliptical peak shape aligned vertically. The later gives symmetry axes at  $\pm 45^\circ$ , and lobes of equal amplitudes, with a “cushion-shaped” CBS peak. When a  $B$  field is applied [Fig. 12(B)] in the  $l \perp l$  channel, the symmetry axes remain  $\pm 45^\circ$  but one or the other pair of lobes is favored depending on the sign of  $\Phi$ . We thus observe that the CBS peak is tilted by  $45^\circ$  *independently* of the magnitude of  $B$  ( $\neq 0$ ), but that it flips by  $90^\circ$  when we reverse the sign of  $B$  and thus of  $\Phi$ . This discussion is valid for  $\delta = 0$ . For  $\delta \neq 0$ , one of the circular components of the induced dipole is favored, and the radiation pattern becomes isotropic [Fig. 12(C)].

Another interesting magneto-optical effect is the so-called photonic Hall effect, predicted and later observed by van Tiggelen *et al.*<sup>40</sup> Its manifestation is an asymmetry in the diffuse intensity in the standard Hall configuration  $k_{in} \perp B \perp k_{out}$ . However, for Rayleigh (point-like) scatterers, this effect vanishes and the asymmetry only shows in the *collective* radiation pattern. In the simplest case of two scatterers, the asymmetry arises from the successive Faraday rotations breaking time-reversal symmetry.<sup>41</sup> For a macroscopic assembly of scatterers, this results in photonic Hall effect much smaller than the average diffuse intensity (by at least  $1/k\ell$ ). Still, numerical simulations indicate that it should be observable in sufficiently dense cold atomic vapors.<sup>41</sup>

### 4.3. Atomic motion

As already discussed in Sec. 3, the residual atomic motion is responsible for some frequency redistribution affecting the transport, which, strictly speaking, can no longer be considered diffusive. What is the impact of the residual Doppler broadening on the coherence of the transport? To answer this question, we performed the experiment described in Fig. 13. Starting from our coldest sample ( $T = 40 \mu\text{K}$ ), we increased gradually the temperature by applying an intense, near-resonant optical molasse. The CBS enhancement was measured for temperatures in the  $40 \mu\text{K}$ - $25 \text{ mK}$  range. This corresponds to a 1D *rms* velocity  $6 \text{ cm/s} < v < 4 \text{ m/s}$ , and a Doppler spread  $0.01\Gamma < kv < 0.85\Gamma$ . For each temperature, the number of atoms in the cloud was adjusted to maintain the optical thickness at a roughly fixed value  $b \approx 13$ .

As can be seen, the CBS enhancement decreases rapidly: the cone height has dropped by a factor 2 for  $kv/\Gamma \simeq 0.15$ , where the Doppler broadening is still well below the natural width.<sup>42</sup> The lines correspond to MC simulations assuming either a Gaussian (dashed line) or a Lorentzian (solid line) velocity distribution. These choices were motivated by the observation of various shapes in the experiment.

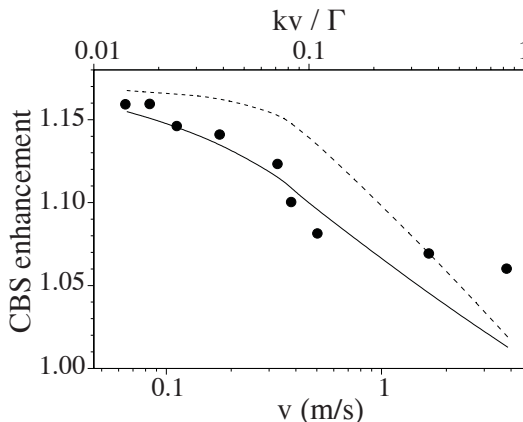


Fig. 13. Atomic motion and coherent transport. We record the CBS enhancement in the  $h \perp h$  channel, as a function of the temperature of the cloud. The optical thickness is fixed at  $\approx 13$ . A rapid decrease of the interference is observed when the *rms* atomic velocity is increased. The dashed and solid lines are MC simulations assuming Gaussian and Lorentzian velocity distributions respectively.

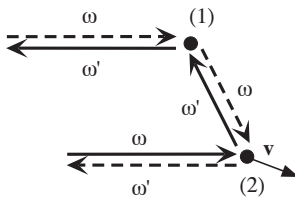


Fig. 14. Role of atomic motion in CBS. We consider a double-scattering picture. Due to the Doppler effect, some frequency redistribution occurs but the outgoing frequency is the same for both reversed paths. However, atom 1 scatters photons at different frequencies  $\omega$  and  $\omega'$  which results in different *amplitudes* for the reversed processes, and thus in a reduced interference contrast.

Although none fits the data in a completely satisfactory fashion, the overall agreement is acceptable. The mechanism for interference reduction is illustrated in Fig. 14. The Doppler effect introduces a frequency difference between “direct” and “reverse” paths *inside* the sample (note that the *outgoing* frequencies are equal). Because the atomic response is highly frequency-dependent, this will induce different (complex) amplitudes for these paths and thus a reduced contrast.<sup>43</sup> This “frequency domain” interpretation has its time domain counterpart, which was used e.g. in Ref. 44 for the case of non-resonant scatterers. Due to the motion of scatterers during the time it takes for the light to travel along a multiple scattering path, photons travelling along “reverse” paths will exit the medium at a different time. The interference is preserved if this time delay is smaller than a wave period, or alternatively if the corresponding path length difference is smaller than  $\lambda$ . The main difference between our situation and that of Ref. 44 is our extremely sharp

resonance, which enhances the impact of the small residual velocity. For non-resonant scatterers moving at non-relativistic velocities, the motion-induced decoherence is quite negligible although the Doppler frequency redistribution can be used to select the number of scattering events.<sup>45</sup>

Going back to the frequency argument, we can derive an analytical expression for the interference contrast in the regime of frequency diffusion  $bkv < \Gamma$  discussed in Sec. 3:<sup>42</sup>

$$\frac{C}{L}(N) = e^{-\frac{N^3}{3} \left(\frac{kv}{\Gamma}\right)^2}. \quad (7)$$

This expression, which is equivalent to that of Ref. 44 when replacing  $c$  by  $v_{tr}$ , shows that the cumulative effect of successive scattering events leads to a very strong cut-off on the scattering orders participating to coherent transport. Despite the non-exponential decay with  $N$ , one can tentatively define a coherence length using  $C/L(N_\phi) = e^{-1}$ . We then obtain:

$$\frac{L_\phi}{\ell} = \left(\frac{3kv}{\Gamma}\right)^{-1/3}. \quad (8)$$

For our lowest temperature of 40  $\mu\text{K}$ , we find  $L_\phi \approx 3\ell$ . It is in principle possible to further cool the atomic cloud, but two problems arise. First, we see (Eq. (8)) that the coherence length increases very slowly when reducing the velocity spread: decreasing  $v$  by one order of magnitude (i.e. the temperature by 2 orders of magnitude) only improves  $L_\phi$  by a factor  $\approx 2$ . Second, if the velocity spread is reduced below the *recoil velocity* corresponding to the momentum exchange between atom and photon during one scattering event, the frequency redistribution will then be determined by the recoil  $v_r$  and not the temperature. This situation can be obtained by e.g. cooling Sr<sup>88</sup> atoms to the recoil limit using the narrow 689 nm transition,<sup>46</sup> and then using the broad 461 nm transition for the CBS experiment. The impact of the recoil on CBS by two trapped atoms as been studied theoretically in Ref. 47. This impact for a realistic situation (an optically-thick cloud of atoms cooled below the recoil limit) remains to be evaluated. However, one can tentatively extrapolate the above discussion on the residual velocity distribution to the case of recoil-induced decoherence, by substituting  $v_r$  to  $v$  in Eq. (8). Since the recoil velocity is 6 mm/s for our transition of Rb<sup>85</sup> (one order of magnitude below our current velocity spread), we can then expect a gain of at most a factor 2 on the coherence length ( $L_\phi \approx 6\ell$ ) by cooling the atoms to the recoil limit. If this extrapolation is correct, Eq. (8) shows that  $L_\phi/\ell \propto (m\Gamma\lambda^2)^{1/3}$ , where  $m$  is the mass of the considered atom,  $\lambda$  the transition wavelength and  $\Gamma$  its natural width. Heavy atoms with wide transitions at large wavelengths are thus more favorable. The recoil limitation could in principle be overcome<sup>48</sup> by pinning the atoms into deep potential wells (Lamb–Dicke regime), like e.g. in an intense far-detuned optical speckle field.

#### 4.4. Nonlinear regime

The interplay between localization effects and nonlinearities opens a vast domain of investigation with very rich physics. Cold atomic gases in disordered optical potentials, where the contact interaction can be tuned e.g. via Feshbach resonances, constitutes an attractive realization to investigate such phenomena. It is also relevant for the physics of random lasers, disordered scattering samples with gain which have been the subject of an intense scrutiny for the past decade.<sup>49</sup> Atomic gases are well-known for their strong nonlinear behavior, which can be simply observed by increasing the light intensity. Some manifestations of this nonlinear behavior have been observed in our group, such as self-lensing<sup>50</sup> or four-wave mixing.<sup>51</sup> We study in this section how the nonlinear scattering properties affect the CBS interference.

For a two-level atom, the nonlinear response to an applied electromagnetic field is due to the saturation of the transition, which occurs when half the population is in the excited state. The degree of saturation is quantified by the *saturation parameter*:

$$s = \frac{I/I_{sat}}{1 + 4(\delta/\Gamma)^2}, \quad (9)$$

where  $I_{sat}$  is a saturation intensity typical of the considered atomic transition (1.6 mW/cm<sup>2</sup> for Rubidium). For non-negligible values of  $s$  (compared to 1), part of the photons are scattered *inelastically* by the atom due to vacuum fluctuations. The inelastic scattered light spectrum is determined by both  $s$  and  $\delta$ , and exhibits a 3-peaks shape known as the Mollow triplet.<sup>52</sup> The ratio of inelastic to elastic scattering rates is  $s$ , thus elastic scattering dominates at  $s < 1$  while inelastic scattering dominates for  $s > 1$ .

Inelastic scattering results in frequency redistribution, thus we expect a loss of CBS interference contrast from quite the same argument as used in Sec. 4.3 for Doppler redistribution. Figure 15 illustrates the simplest double-scattering picture, in a perturbative approach where we consider a *single* inelastic scattering event per multiple scattering path.<sup>53</sup> In this picture where we assume identical outgoing frequencies, the occurrence of inelastic scattering does not suppress the interference but reduces its contrast due to the different amplitudes for the reversed paths. This

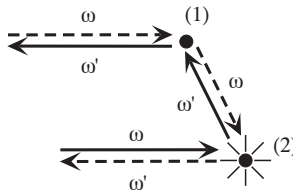


Fig. 15. Role of inelastic scattering in CBS. We consider a perturbative, double-scattering picture. A single inelastic scattering occurs per multiple scattering path, seen here at atom 2. Since atom 1 scatters photons at different frequencies  $\omega$  and  $\omega'$ , the amplitudes for the reversed processes are different, resulting in a reduced interference contrast.

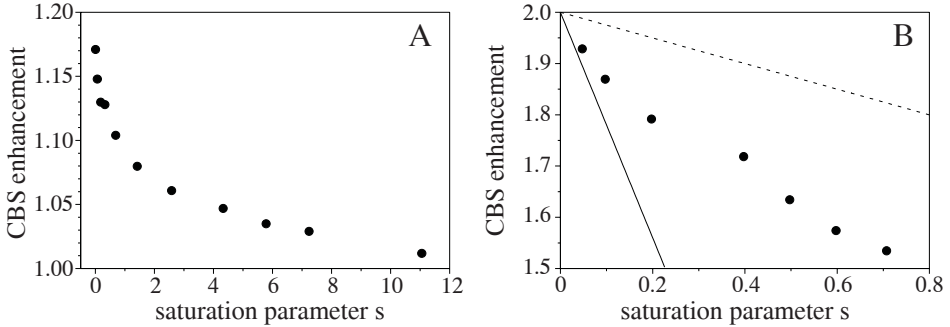


Fig. 16. Decoherence in the nonlinear regime. We record (symbols) the CBS enhancement as a function of the saturation parameter ( $\delta = 0$ ) for: (A) a cold cloud of Rb<sup>85</sup> of optical thickness  $b \approx 10$  ( $h \perp h$ ), (B) a cold cloud of Sr<sup>88</sup> of optical thickness  $b = 2.5$  ( $h \parallel h$ ). The dashed line in (B) is a 2-atom, non-perturbative calculation. The solid lines in (B) is a perturbative calculation valid for optically-thick samples (see text).

non-zero contribution of inelastic scattering was also noted in the limit of large saturations ( $s \gg 1$ ) using a non-perturbative approach.<sup>54</sup> We may thus re-write Eq. (4) for the CBS enhancement the form:

$$\eta = 1 + \frac{C_{el} + C_{in}}{S + L_{el} + L_{in}}, \quad (10)$$

with  $C_{el}/L_{el} = 1$  and  $C_{in}/L_{in} < 1$ . Note however that this simple picture is valid for double scattering only, as will be further discussed later.

The reduction of CBS interference in the nonlinear regime was first observed in our group on cold clouds of Rb<sup>85</sup> [see Fig. 16(A)] and Sr<sup>88</sup> [Fig. 16(B)].<sup>55</sup> The group of M. Havey later also reported a decreased interference when saturation is increased.<sup>56</sup>

In Fig. 16(B) a linear decrease  $\eta \simeq 2 - 0.6 \times s$  is observed for moderate saturations  $0 < s < 0.7$ . In the case of Rb<sup>85</sup> [Fig. 16(A)], the decrease rate is similar with a reduction of the CBS peak height by a factor  $\approx 2$  at  $s = 0.8$ . These decreases are faster than expected from the 2-atom models<sup>53</sup> and<sup>54</sup> [dashed line in Fig. 16(B)].

The discrepancy between experiments and 2-atom models is not *a priori* surprising, since several additional effects are expected to arise in the case of optically-thick samples. One example is the inhomogeneous intensity distribution to which atoms are subjected. The local field at a given point inside the cloud is the sum of the “coherent” (i.e. incident) field attenuated by its passage through the front layer and the *diffuse* field radiated by all other atoms. The first term can be computed using the nonlinear version of Beer–Lambert’s law, assuming that the influence of the diffuse light on the local saturation can be neglected. For optically-thick clouds  $b > s$ , the coherent component exhibits a large spatial variation with maximal values at the front surface and a vanishing intensity deep inside the sample. The evaluation of the diffuse component requires to solve a “nonlinear diffusion equation”, with the further complication that inelastic scattering changes the light mean-free path,

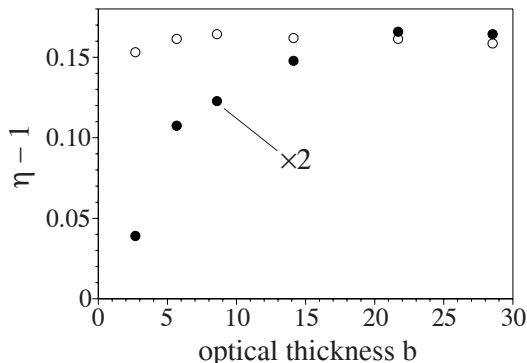


Fig. 17. Role of optical thickness in nonlinear CBS. We record the CBS peak height  $\eta - 1$  for  $\text{Rb}^{85}$  in the  $h \perp h$  channel ( $\delta = 0$ ), as a function of the optical thickness of the cloud in the linear regime  $s = 0.06$  (open circles), and the nonlinear regime  $s = 2$  (solid circles,  $\times 2$ ). A much stronger variation is observed in the nonlinear case.

which in turn affects the diffusive modes. In general, the spatial variation of the diffuse modes is rather weak. The resulting total intensity can thus exhibit a quite inhomogeneous distribution inside the sample. An experimental evidence for the role played by this inhomogeneous intensity distribution is shown in Fig. 17.

We record the CBS peak height  $\eta - 1$  for  $\text{Rb}^{85}$  as a function of the optical thickness (measured at  $s \ll 1$ ), in the linear regime  $s = 0.06$  (open circles) and in the nonlinear regime  $s = 2$  (solid circles). In the latter, the peak height has been multiplied by 2 to ease the comparison: at large optical thickness, one has  $\eta \approx 1.16$  in the linear case and  $\eta \approx 1.08$  in the nonlinear one. We see that in the linear regime the CBS peak height depends only weakly on the optical thickness (7% relative variation), as already discussed in Sec. 4.2 [Fig. 10(B)]. On the contrary, in the nonlinear case, we observe a much stronger variation with a four-fold increase. Two mechanisms can conspire to produce this effect. Both rely on the inhomogeneous intensity distribution discussed above: very crudely, for  $1 < s < b$  the sample is composed of a front saturated layer, followed by a back layer where the incident mode intensity is strongly attenuated yielding  $s < 1$  (linear case). In this regime, further increasing  $b$  amounts to increasing the proportion of atoms exposed to a low saturation. This has two consequences. First, saturated atoms are expected to contribute less to CBS than unsaturated ones, which yields an increasing  $\eta(b)$ . Second, saturated atoms produce mainly single scattering (“bleaching”), while the optically-thick back layer is responsible for most of the multiple scattering contribution. Thus, increasing  $b$  reduces the overall proportion of single scattering, which also yields an increasing  $\eta(b)$ . In the absence of reliable models for the Rb case of Fig. 17, it is difficult to estimate the relative contributions of these two mechanisms. Preliminary observations on Sr, where single scattering can be filtered out, do not show such a large variation which suggests a dominant role of single scattering in the evolution of Fig. 17.

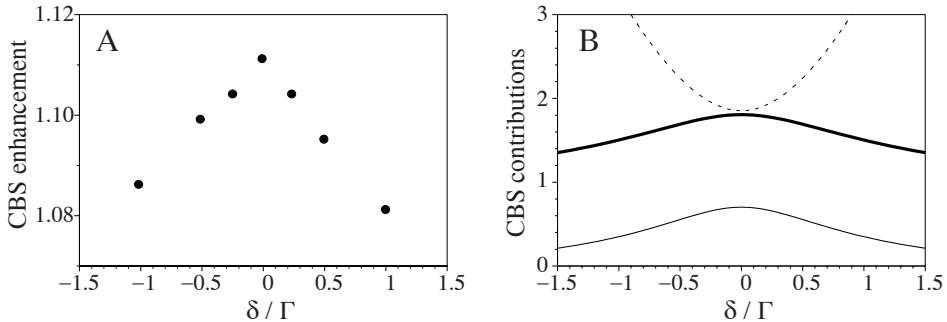


Fig. 18. Role of the light detuning in saturated CBS. We record in (A) the CBS peak as a function of the detuning from resonance  $\delta$  of the incident light ( $\text{Rb}^{85}$ ,  $h \perp h$ ). For each detuning value, the light intensity and number of trapped atoms are adjusted to maintain fixed saturation  $s = 0.8$  and transmission  $T = 0.13$ . The interpretation (see text) of this behavior is illustrated in (B) with the results of a 2-atom calculation ( $0 \rightarrow 1$  transition) showing: the inelastic-to-elastic ratio  $L_{in}/L_{el}$  (dashed line), the inelastic contrast  $C_{in}/L_{in}$  (thin solid line) and the total CBS enhancement (bold solid line).

In addition to the effects discussed above which should arise in the case of optically-thick samples, more intriguing phenomena occur when considering more than two atoms.<sup>57</sup> Indeed, if one now allows more than one elastic scattering in addition to the single inelastic scattering, one then has to consider interferences between *three amplitudes* instead of two. This allows in principle the possibility to observe a CBS enhancement factor  $> 2$  (with a maximal value of 3), provided that the elastic component can be filtered out.<sup>57</sup> However, in the absence of such a filtering, the 3-amplitude term has the effect of further *decreasing* the CBS enhancement. As a consequence, the decay of  $\eta$  with increasing  $s$  is faster for larger optical thicknesses. This is illustrated by the solid line in Fig. 16(B), which corresponds to a MC simulation ( $b = 2.5$ ) along the lines of Ref. 57. The observed decrease, much faster than in the 2-atom case (dashed line), is attributed to the three-amplitude mechanism. We note that the theory is still off the experimental data, but we emphasize that this perturbative approach is only valid in the limited range  $sb^2 \ll 1$ . More careful experiments are required in this regime to quantitatively check this theory.

In the regime of linear CBS, the detuning of the incident light plays no intrinsic role i.e. it just affects the optical thickness of the cloud, in the same way a change of the number of atoms would (as long as additional off-resonant transitions can be neglected, see Fig. 10(B)). In the nonlinear regime, this picture changes, because the *spectrum* of the scattered light depends both on the saturation  $s$  and on the detuning  $\delta$ . This intrinsic role of the detuning can be measured experimentally as illustrated in Fig. 18(A).

The CBS enhancement factor is measured as a function of  $\delta$ . For each value of  $\delta$ , the light intensity and number of trapped atoms were adjusted to maintain a *fixed saturation*  $s = 0.8$  and a *fixed transmission*  $T = 0.13$ . If one neglects the influence

of the diffuse light in the local saturation parameter, these precautions amount to fixing the profile of excitation inside the sample. Despite this, we observe a definite effect of the detuning, with a decreasing CBS interference when  $|\delta|$  increases. Note that in the linear regime, the enhancement would be independent of  $\delta$  in this experiment. This behavior is also predicted by a 2-atom calculation of B. Grémaud (Fig. 18(B)) and can be understood qualitatively as follows. The inelastic spectrum of the light scattered by a single atom is typically described by the Mollow triplet,<sup>52</sup> with three peaks centered at 0,  $\delta$  and  $2\delta$  respectively. In the  $\delta = 0$  case, all three peaks are superimposed and centered on resonance. The scattered light also has an elastic component, which by definition is a Dirac peak centered at the incident light detuning  $\delta$ . In our naive 2-atom picture, the CBS interference is due to the elastic contribution (maximal contrast) and the inelastic contribution (reduced contrast). The total CBS contrast thus depends on the elastic-to-inelastic ratio, and on the contrast of the inelastic contribution. The later depends on the amount of frequency redistribution  $\Delta\omega$  introduced by inelastic scattering (see Fig. 15). Because one peak of the Mollow triplet is always centered on resonance and thus dominates the other Mollow components, one has  $\Delta\omega \approx \delta$ . Thus, increasing  $|\delta|$  has two consequences: first, the inelastic-to-elastic ratio increases (Fig. 18(B), dashed line) because the elastic light is detuned while the inelastic peak remains on resonance. Second, the inelastic contrast decreases (Fig. 18(B), thin solid line) because  $\Delta\omega$  increases. Both effects add up to decrease the total enhancement factor (bold solid line). It is worth mentioning here that the actual situation is in principle much more complicated (even for just two atoms) due again to the internal structure of the Rb atom. Indeed, the spectrum of the light scattered by an atom with a Zeeman degeneracy exhibits some peculiar features which are qualitatively different from that of the  $0 \rightarrow 1$  atom described by the Mollow triplet.<sup>58</sup>

As already mentioned, no theoretical treatment is at present able to describe the experiments reported here, namely in the regime of both  $s$  and  $b > 1$ . Some recent efforts have permitted us to extend the analysis to large saturations and optical thicknesses,<sup>59</sup> but without accounting for inelastic scattering. This could in principle be achieved using the approach of Ref. 60. Many intriguing questions remain open, in particular regarding the interplay of multiple scattering and gain in connection with the physics of random lasers.

## 5. Conclusion

We have presented in this paper a review of our work on the quasi-diffusive transport of near-resonant light in cold atomic vapors. The unusual properties of these media, such as e.g. their strong resonance and nonlinear response, have allowed us to observe some interesting new regimes and physics. For instance, the use of laser-cooled atoms allowed us to study radiation trapping in a new “frequency diffusion” regime, bridging the gap between the usual elastic and Doppler regimes of transport. Due to the strongly resonant and very monodisperse ensemble of scatterers, we

observed an unprecedented energy transport velocity of  $\approx 10^{-5}c$ . Using the coherent backscattering interference as a probe of coherent transport, we have identified three distinct decoherence mechanisms (internal structure, atomic motion, nonlinearity). From this analysis, we expect for ultracold vapors the recoil-induced decoherence to ultimately limit the coherence length to rather small values  $< 10\ell$  ( $\approx 6\ell$  for Sr<sup>88</sup>). We are currently upgrading our experiments to approach the theoretical threshold  $k\ell = 1$  for Anderson localization in 3D. One may argue that the transition to localization will not be observable if  $L_\phi < L_{loc}$ , where  $L_{loc}$  is the localization length. In 3D the localization length is typically much larger than the mean-free-path  $\ell$  ( $L_{loc}/\ell \approx 10^3 - 10^4$  in<sup>9</sup>). It thus seems extremely difficult to reach the regime  $L_{loc} < L_\phi$  in cold vapors, which questions the possibility to observe 3D Anderson localization in such systems.

## Acknowledgment

We thank the CNRS, LNE and PACA Region for financial support.

## References

1. P. W. Anderson, *Phys. Rev.* **109** (1958) 1492.
2. E. Larose, L. Margerin, B. A. van Tiggelen and M. Campillo, *Phys. Rev. Lett.* **93** (2004) 048501.
3. J. de Rosny, A. Tourin and M. Fink, *Phys. Rev. E* **64** (2001) 066604.
4. E. Akkermans, G. Montambaux, J.-L. Pichard and J. Zinn-Justin (eds.), *Mesoscopic Quantum Physics* (Elsevier Science B.V., North Holland, Amsterdam, 1995).
5. R. C. Kuhn, C. Miniatura, D. Delande, O. Sigwarth and C. A. Müller, *Phys. Rev. Lett.* **95** (2005) 250403.
6. A. A. Chabanov and A. Z. Genack, *Opt. Photon. News* **13** (2002) 25.
7. M. P. van Albada and A. Lagendijk, *Phys. Rev. Lett.* **55** (1985) 2692; F. Scheffold and G. Maret, *ibid.* **81** (1998) 5800.
8. D. Wiersma *et al.*, *Nature (London)* **390** (1997) 671.
9. M. Störzer, P. Gross, C. M. Aegerter and G. Maret, *Phys. Rev. Lett.* **96** (2006) 063904; C. M. Aegerter, M. Störzer and G. Maret, *Europhys. Lett.* **75**(4) (2006) 562.
10. G. Labeyrie, F. de Tomasi, J.-C. Bernard, C. A. Müller, C. Miniatura and R. Kaiser, *Phys. Rev. Lett.* **83** (1999) 5266.
11. C. Kenty, *Phys. Rev.* **42** (1932) 823.
12. T. Holstein, *Phys. Rev.* **72** (1947) 1212.
13. A. F. Molisch and B. P. Oehry, *Radiation Trapping in Atomic Vapors* (Clarendon Press, Oxford, 1998).
14. A. Fioretti *et al.*, *Opt. Commun.* **149** (1998) 415.
15. G. Labeyrie, L. Vaujour, C. A. Müller, D. Delande, C. Miniatura, D. Wilkowski and R. Kaiser, *Phys. Rev. Lett.* **91** (2003) 223904.
16. G. Labeyrie, R. Kaiser and D. Delande, *Appl. Phys. B* **81** (2005) 1001.
17. A. Lagendijk and B. A. van Tiggelen, *Phys. Rep.* **270** (1996) 143.
18. Y. Shimizu *et al.*, *Phys. Rev. Lett.* **89** (2002) 233001.
19. M. P. van Albada, B. A. van Tiggelen, A. Lagendijk and A. Tip *Phys. Rev. Lett.* **66** (1991) 3132.
20. S. Balik *et al.*, *Phys. Rev. A* **72** (2005) 051402(R).

21. L. V. Hau *et al.*, *Nature (London)* **397** (1999) 594.
22. Y. Kuga and A. Ishimaru, *J. Opt. Soc. Am. A* **1**(8) (1984) 831; P. L. Wolf and G. Maret, *Phys. Rev. Lett.* **55** (1985) 2696; M. P. van Albada and A. Lagendijk, *ibid.* **55** (1985) 2692.
23. P. Kulatunga, C. I. Sukenik, S. Balik, M. D. Havey, D. V. Kupriyanov and I. M. Sokolov, *Phys. Rev. A* **68** (2003) 033816.
24. T. Jonckheere, C. A. Müller, R. Kaiser, C. Miniatura and D. Delande, *Phys. Rev. Lett.* **85** (2000) 4269.
25. C. Miniatura, C. A. Müller, Y. Lu, G. Wang and B.-G. Englert, *Phys. Rev. A* **76** (2007) 022101.
26. C. A. Müller, T. Jonckheere, C. Miniatura and D. Delande, *Phys. Rev. A* **64** (2001) 053804.
27. C. A. Müller, C. Miniatura, L. Akkermans and G. Montambaux, *J. Phys. A: Math. Gen.* **38** (2005) 7807.
28. Y. Bidel, B. Klappauf, J.-C. Bernard, D. Delande, G. Labeyrie, C. Miniatura, D. Wilkowski and R. Kaiser, *Phys. Rev. Lett.* **88** (2002) 203902.
29. G. Labeyrie, D. Delande, C. A. Müller, C. Miniatura and R. Kaiser, *Europhys. Lett.* **61** (2003) 327.
30. D. Wilkowski, Y. Bidel, T. Chanelière, D. Delande, T. Jonckheere, B. Klappauf, G. Labeyrie, C. Miniatura, C. A. Müller, O. Sigwarth and R. Kaiser, *J. Opt. Soc. Am. B* **21** (2004) 183.
31. G. Labeyrie, D. Delande, C. A. Müller, C. Miniatura and R. Kaiser, *Phys. Rev. A* **67** (2003) 033814.
32. D. V. Kupriyanov, I. M. Sokolov, P. Kulatunga, C. I. Sukenik and M. D. Havey, *Phys. Rev. A* **67** (2003) 013804.
33. C. A. Müller, C. Miniatura, D. Wilkowski, R. Kaiser and D. Delande, *Phys. Rev. A* **72** (2005) 053405.
34. O. Sigwarth, G. Labeyrie, T. Jonckheere, D. Delande, R. Kaiser and C. Miniatura, *Phys. Rev. Lett.* **93** (2004) 143906.
35. F. A. Erbacher, R. Lenke and G. Maret, *Europhys. Lett.* **21** (1993) 551; B. A. van Tiggelen, R. Maynard and T. M. Nieuwenhuizen, *Phys. Rev. L* **53** (1996) 2881.
36. F. Pierre, A. B. Gougam, A. Anthore, H. Pothier, D. Esteve and N. O. Birge, *Phys. Rev. B* **68** (2003) 085413.
37. G. Labeyrie, C. Miniatura and R. Kaiser, *Phys. Rev. A* **64** (2001) 033402.
38. G. Labeyrie, C. Miniatura, C. A. Müller, O. Sigwarth, D. Delande and R. Kaiser, *Phys. Rev. Lett.* **89** (2002) 163901.
39. M. P. van Albada, M. B. van der Mark and A. Lagendijk, *Phys. Rev. Lett.* **58** (1987) 361.
40. B. A. van Tiggelen, *Phys. Rev. Lett.* **75** (1995) 424; G. L. J. A. Rikken and B. A. van Tiggelen, *Nature* **381** (1996) 54.
41. B. Grémaud, private communication.
42. G. Labeyrie, D. Delande, R. Kaiser and C. Miniatura, *Phys. Rev. Lett.* **97** (2006) 013004.
43. D. Wilkowski *et al.*, *Physica B (Amsterdam)* **328** (2003) 157.
44. A. A. Golubentsev, *Sov. JETP* **59** (1984) 26.
45. M. Lesaffre, M. Atlan and M. Gross, *Phys. Rev. Lett.* **97** (2006) 033901.
46. H. Katori, T. Ido, Y. Isoya and M. Kuwata-Gonokami, *Phys. Rev. Lett.* **82** (1999) 1116.
47. C. Wickles and C. A. Müller, *Europhys. Lett.* **74**(2) (2006) 240.
48. T. Ido and H. Katori, *Phys. Rev. Lett.* **91** (2003) 053001.

49. H. Cao, *J. Phys. A: Math. Gen.* **38** (2005) 10497.
50. G. Labeyrie *et al.*, *Eur. Phys. J. D* **22**(3) (2003) 473; G. Labeyrie *et al.*, *ibid.* **41** (2007) 337.
51. G.-L. Gattobigio, F. Michaud, J. Javaloyes, J. W. R. Tabosa and R. Kaiser, *Phys. Rev. A* **74** (2006) 043407; F. Michaud, G.-L. Gattobigio, J. W. R. Tabosa and R. Kaiser, *J. O. S. A. B* **24** (2007) A40.
52. B. R. Mollow, *Phys. Rev. A* **5** (1972) 2217.
53. T. Wellens, B. Grémaud, D. Delande and C. Miniatura, *Phys. Rev. A* **70** (2004) 023817.
54. V. Shatokin, C. A. Müller and A. Buchleitner, *Phys. Rev. Lett.* **94** (2005) 043603; V. Shatokin, C. A. Müller and A. Buchleitner, *Phys. Rev. A* **73** (2006) 063813.
55. T. Chanelière, D. Wilkowski, Y. Bidet, R. Kaiser and C. Miniatura, *Phys. Rev. E* **70** (2004) 036602.
56. S. Balik, P. Kulatunga, C. I. Sukenik, M. D. Havey, D. V. Kupriyanov and I. M. Sokolov, *J. Mod. Optics* **52** (2005) 2269; D. V. Kupriyano, I. M. Sokolov, C. I. Sukenik and M. D. Havey, *Laser Phys. Lett.* **3** (2005) 223.
57. T. Wellens, B. Grémaud, D. Delande and C. Miniatura, *Phys. Rev. A* **73** (2006) 013802.
58. B. Gao, *Phys. Rev. A* **50** (1994) 4139.
59. T. Wellens and B. Grémaud, arXiv cond-mat:0707.1956 (2007).
60. B. Grémaud, T. Wellens, D. Delande and C. Miniatura, *Phys. Rev. A* **74** (2006) 033808.